

## On the vibration suppression of power lines using mobile damping robots

Paul Kakou, Mohammad Bukhari, Jiamin Wang, Oumar Barry\*

*Department of Mechanical Engineering, Virginia Tech, Blacksburg, VA 24060, United States*



### ARTICLE INFO

**Keywords:**

Moving absorber  
Power lines  
Antinode tracking  
Damping robot

### ABSTRACT

Fixed passive tuned vibration absorbers (TVA) are ineffective in controlling wind induced vibration of continuous systems (e.g., power lines). This is because fixed passive TVAs are not only narrowband, but they are also unable to adapt to changing wind characteristics, and thus are unable to reposition themselves at antinodes of the vibrating loop. To tackle this issue, this paper proposes a mobile vibration absorber (i.e., mobile damping robot) capable of self-adjustment to antinodes. The study focuses on power lines vibration suppression, but it can be extended to other continuous systems. The mobile damping robot is connected to a single conductor that is subjected to a pretension and a wind force. The governing equations of motion are obtained using Hamilton's principle. A control force is incorporated in the mathematical formulation for driving the robot to the antinode location based on the wind excitation frequency. Also, the two-way nonlinear coupling between the robot and cable is considered. Numerical simulations indicate that the mobile damping robot significantly improves the vibration suppression of the power line. Parametric studies are carried out to determine the influence of key design parameters on the performance of the mobile damping robot.

### 1. Introduction

Buildings, bridges, overhead transmission lines and other continuum systems are essential as human strive for high-quality lives. However, these systems are subject to undesirable vibrations that lead to fatigue damages. Wind-induced vibration (WIV) is an example of undesirable vibration for engineering structures, such as suspended roofs, guyed lattice towers, wind turbines, spacecraft, power lines, and cable-stayed bridges. For overhead power lines, these oscillatory motions typically take the form of Aeolian vibration caused by vortex shedding. Aeolian vibration frequency generally varies between 3 and 150 Hz, and the peak-to-peak amplitude can be the same as the cable diameter [1–6]. Left uncontrolled, WIV can lead to power lines failure, thereby undermining public safety and resulting in considerable economic loss. The Department of Energy (DOE) reported that weather-related annual outage costs were estimated to be between \$18 and \$33 billion [7]. While WIV is only responsible for a small percentage of this, the costs are still enormous. In March 2017, DTE Energy Co. reported that a WIV caused power outage to more than 4,000 customers [8]. Similar power outages due to WIV were reported in Ontario leaving millions of customers without power.

To minimize the damages, tuned vibration absorbers (TVAs) have been utilized for many years. They are qualified as passive, semi-active

and active TVAs [9,10]. Passive TVAs suppress vibrations by impedance coupling using a mass-spring system. Passive TVAs are favored for their structural simplicity and good stability, but they are significantly limited in applications where the primary structure encounters broadband disturbances. Moreover, the deterioration of passive TVAs structural parameters overtime decreases their efficiency. To overcome passive TVAs limitations, active TVAs have been implemented. Active absorbers consist of sensors and actuators coupled with a controller that drives the absorber to suppress the vibration of the system. However, the performance of active absorbers suffers from control-induced instability. Recently, emphasis has been given to semi-active absorbers, which combine the benefits of passive and active TVAs by using a control scheme that tunes the passive device parameters such as the stiffness of the absorber. Passive, active, and semi-active TVAs have been used to control vibrations of manufacturing tools [11–13], buildings [14], offshore platforms [15], power lines [16], and many other engineering systems and structures [17–19].

In the literature, several authors have investigated vibration suppression of continuous systems [20–30]. TVAs are currently used to suppress the vibration of these systems. For instance, Stockbridge dampers are used to suppress overhead transmission lines vibrations [31]. The effectiveness of Stockbridge dampers (i.e., fixed TVAs) is dependent on the number of resonant frequency they exhibit (i.e.,

\* Corresponding author.

E-mail address: [obarry@vt.edu](mailto:obarry@vt.edu) (O. Barry).

absorber's natural frequency matching excitation frequency), and their locations on the conductor [32,2,3,4,33,5,34]. The ideal location is the antinode of the vibrating loop. However, because vibration loop length depends on wind velocity, the assurance of relative position of a fixed absorber with respect to an antinode is practically impossible. There are numerous studies that optimize the placement of fixed absorbers closer to antinodes [35,36,2], but none guarantee reasonable performance at every wind frequency. This is primarily because the change in frequency with varying wind speed can cause the location of the absorber to coincide with a node, thus resulting in poor performance. This challenge can be overcome using mobile damping robots capable of adapting to the wind characteristics and automatically re-position themselves to antinodes. A few studies in the literature have already explored the idea of moving dampers. For instance, Fei et al. [37] discussed the advantages of using a moving damper to critically suppress the vibrations of a work-piece during milling. Wang et al. [38] studied the vibration suppression of a rigid body by using an absorber that slides across a groove. These works have further motivated Bukhari et al. [39,6] to study a mobile damper for controlling wind-induced vibration of overhead transmission lines.

It should be noted that the study in [39] did not consider the two-way nonlinear coupling between the mobile damper and the cable. Also, the study in [39] was limited to a defined profile motion based on a known input excitation. The aim in this paper is to address this knowledge gap in order to develop a mobile damping robot (MDR) that adapts its motion profile based on the instant input excitation by using a feedback controller. This is because input excitation varies over a wide range of frequencies (e.g., 3–150 Hz for Aeolian vibrations) in real life applications. The governing equations of motion are derived using Hamilton's principle, and numerical analysis are carried out using MATLAB®. The numerical results are used to demonstrate the improvement in vibration suppression performance of the MDR. Detailed parametric studies are also conducted to determine the role of different key parameters that impact the performance of the robot.

## 2. System description and modeling

This section presents the mathematical derivation of the mobile damping robot attached to a conductor. Fig. 1 shows a prototype of the MDR. The proposed robot is inspired by power lines inspection robots

and our recent patented Aeolian vibration damper [40]. Fig. 2 shows a simplified representation of the mobile device attached to the conductor. The conductor is modeled using Euler-Bernoulli beam theory with a length  $L$ , a mass per unit length  $m$ , a flexural rigidity  $EI$  and a pretension  $T$ . The Aeolian vibration damper of the mobile device is reduced to an equivalent single degree of freedom system [36], which has an in-span mass  $m_r$ , a suspended mass  $m_d$ , a linear spring  $k$ , an equivalent damping coefficient  $c$  and horizontal velocity  $\dot{x}_r$ . The mathematical model of the system can be obtained by first identifying the position vector of the beam, the in-span mass and the suspended absorber given as:

$$\mathbf{r}_b = xi + y(x, t)\mathbf{j} \quad (1)$$

$$\mathbf{r}_r = x_r\mathbf{i} + y(x_r, t)\mathbf{j} \quad (2)$$

$$\mathbf{r}_d = x_r\mathbf{i} + y_d\mathbf{j} \quad (3)$$

where  $r_b$ ,  $r_r$  and  $r_d$  represent the position of the beam, the in-span mass and the absorber, respectively.  $x$  and  $y$  represent the horizontal and vertical position across the beam.  $x_r$  is the location of the robot on the beam, and  $y_d$  is the vertical displacement of the damper.

The time derivatives of the position vectors with respect to time are defined as:

$$\dot{\mathbf{r}}_b = \dot{y}(x, t)\mathbf{j} \quad (4)$$

$$\dot{\mathbf{r}}_r = \dot{x}_r\mathbf{i} + (\dot{y}(x_r, t) + y'(x_r, t)\dot{x}_r)\mathbf{j} \quad (5)$$

$$\dot{\mathbf{r}}_d = \dot{x}_r\mathbf{i} + \dot{y}_d\mathbf{j} \quad (6)$$

The definition of the velocity vectors can be used to formulate the kinetic energy of the system as:

$$E_k = E_{kb} + E_{kr} + E_{kd} \quad (7)$$

where  $E_{kb}$ ,  $E_{kr}$ , and  $E_{kd}$  are the kinetic energy of the beam, the in-span mass, and the absorber, respectively. Each one of these energies may be expressed as:

$$E_{kb} = \frac{1}{2}m \int_0^L (\dot{y}(x, t))^2 dx \quad (8)$$

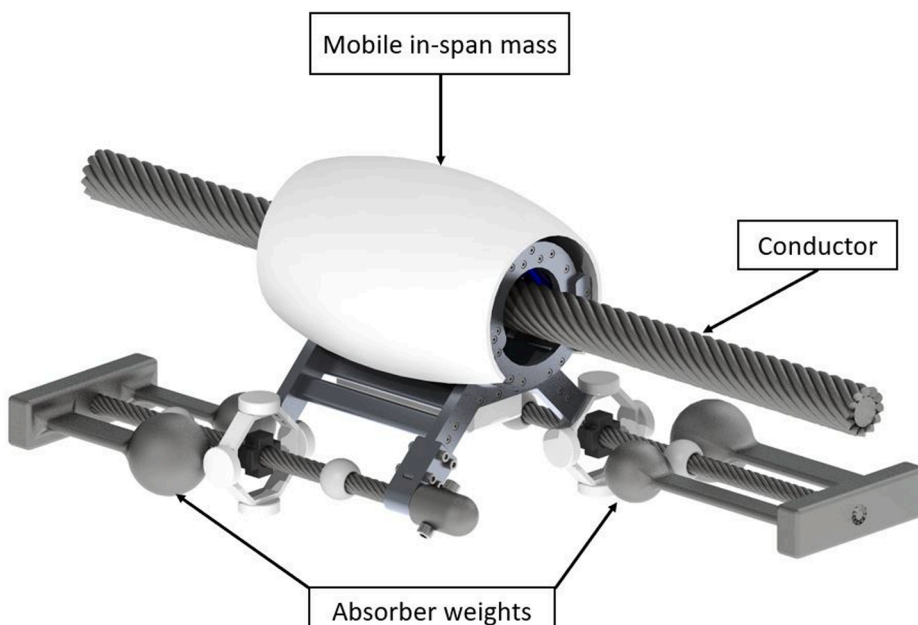


**Fig. 1.** Conceptual design of the MDR attached to a power line cable.

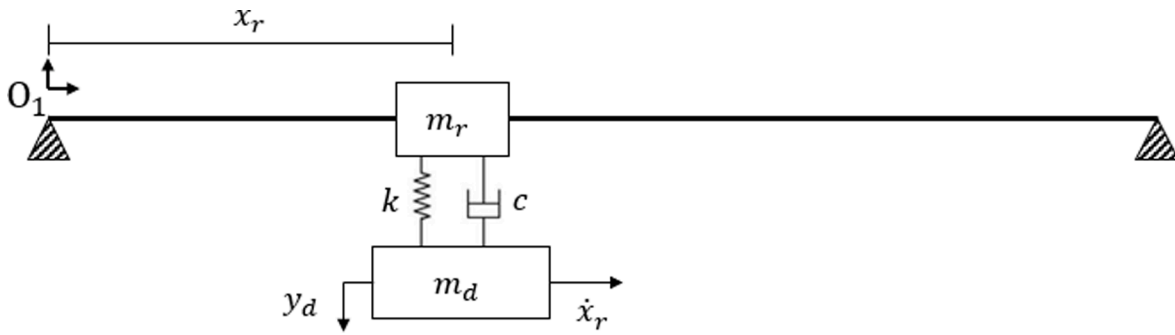


Fig. 2. Schematic of the MDR on the cable.

$$E_{kr} = \frac{1}{2}m_r(\dot{x}_r^2 + (\dot{y}(x_r, t) + \dot{y}(x_r, t)\dot{x}_r)^2) \quad (9)$$

$$E_{kd} = \frac{1}{2}m_d(\dot{x}_r^2 + \dot{y}_d^2) \quad (10)$$

Similarly, the potential energy can be defined for each component of the system. The potential energy of the beam includes the restoring energy generated by the pre-tension and the material elastic properties. Consequently, the total potential energy can be summarized as:

$$V = \frac{1}{2}EI \int_0^L (\ddot{y}(x, t))^2 dx + \frac{1}{2}k(y(x_r, t) - y_d)^2 + \frac{1}{2}T \int_0^L (\dot{y}(x, t))^2 dx \quad (11)$$

Using these energy expressions along with Hamilton's principle, the governing equation of motion of the cable can be expressed as:

$$EIy'''' + m\ddot{y} + Ty'' = F(x, t) - (F_1 + F_2)D(x, t) \quad (12)$$

where  $F(x, t)$  is the wind input force. This wind force is assumed to be uniformly distributed on the conductor and can be expressed as a time sinusoidal function following [41]:

$$F(t) = f_0 \sin(\omega_e t) \quad (13)$$

where  $f_0$  is the amplitude of the wind force as described in [39] and  $\omega_e$  represents the wind excitation frequency.

$F_1$ ,  $F_2$  and  $D(x, t)$  are given as:

$$F_1 = m_r(\ddot{x}_r + (\ddot{y} + 2\dot{y}\dot{x}_r + \ddot{y}\dot{x}_r^2 + y\ddot{x}_r)) \quad (14)$$

$$F_2 = k(y - y_d) + c(\dot{y} + \dot{y}\dot{x}_r - \dot{y}_d) \quad (15)$$

where the non-conservative force due to the damping element is considered.

$$D(x, t) = \delta(x - x_r) \quad (16)$$

The vertical displacement of the mass of the absorber can be expressed as:

$$m_d\ddot{y}_d - F_2 = 0 \quad (17)$$

In this work, the mobile robot actively tracks the antinode. Therefore, the equation of motion of the robot in the horizontal direction can be expressed as:

$$[(m_d + m_r)\ddot{x}_r + m_r(\ddot{y} + 2\dot{y}\dot{x}_r + \ddot{y}\dot{x}_r^2 + y\ddot{x}_r)\dot{y}] = F_c \quad (18)$$

where  $F_c$  represents a PD control force given as:

$$F_c = k_p(r - x_r) + k_d(v_d - \dot{x}_r) \quad (19)$$

where  $k_p$  and  $k_d$  are the proportional and the derivative gain respectively.  $r$  represents the closest antinode location (i.e. position target) while  $v_d$  represents the desired MDR tracking velocity (i.e. velocity

target). To track the antinode, the MDR is equipped with a wind sensor and an accelerometer. The wind sensor helps determine the Strouhal frequency expressed as:

$$f_s = 0.2 \frac{V_w}{D} \quad (20)$$

where  $f_s$  corresponds to the excitation frequency in Hertz.  $V_w$  is the velocity of the wind and  $D$  represents the diameter of the conductor. Considering the case of resonance i.e., once the Strouhal frequency matches a conductor resonant frequency, the position of the antinode can be approximately determined. In this case, the controller generates a signal to the actuator to track the closest antinode. The accelerometer is used to measure the vibration of the conductor and help ensure that the average vibration across the cable is suppressed over time.

In order to discretize the partial differential equation of the system into a system of ordinary differential equations, the solution can be expressed using the Galerkin decomposition method as:

$$y(x, t) = \sum_{r=1}^{\infty} \Phi_r(x)A_r(t) \quad (21)$$

where  $A_r(t)$  are the time functions of the transverse displacement, and  $\Phi_r(x)$  are the normalized eigenfunctions (mode shapes). The eigenfunctions are chosen as the mode shapes of a simply supported beam with tension ([44]) as:

$$\Phi_r(x) = \sqrt{\frac{2}{mL}} \sin((\sqrt{\frac{-T}{2EI}} + \sqrt{\frac{T^2}{4(EI)^2} + \frac{m\omega_r^2}{EI}})x) \quad (22)$$

where the natural frequencies of the bare beam are given by

$$\omega_n = \left(\frac{\pi}{L}\right) \sqrt{\frac{EI}{m}(n^4 + \frac{n^2 TL^2}{\pi^2 EI})} \quad (23)$$

Substituting Eq. (21), into Eq. (12), multiplying by  $\Phi_i(x)$ , integrating over the length of the beam, and applying the orthogonality condition yields

$$\begin{aligned} \ddot{A}_p(t) + m_r[\sum_{r=1}^{\infty} \ddot{A}_r(t)\Phi_r(d) + 2\dot{A}_r(t)\Phi_r(d)v_a \\ + A_r(t)\Phi_r''(d)v_a^2]H_p(t) + 2\zeta\omega_p\dot{A}_p(t) + \omega_p^2A_p(t) \\ + \{k[\sum_{r=1}^{\infty} A_r(t)\Phi_r(d) - y_d(t)] + c[\sum_{r=1}^{\infty} A_r(t)\Phi_r(d) + A_r(t)\Phi_r'(d)v_d \\ - y_d(t)]\}H_p(t) = S_p(t) \end{aligned} \quad (24)$$

Similarly, Eq. (17) and Eq. (19) yield

$$(m_d + m_r)\ddot{x}_r(t) + m_r[\sum_{r=1}^{\infty} \ddot{A}_r(t)\Phi_r(d) - 2\dot{A}_r(t)\Phi_r'(d)x_r]$$

$$+ A_r(t)\Phi_r''(d)\ddot{x}_r^2(t) + A_r(t)\Phi_r'(d)\ddot{x}_r(t)]A_r(t)\Phi_r'(d) \\ = k_p(r - x_r(t)) + k_d(v_d - \dot{x}_r(t)) \quad (25)$$

$$m_d\ddot{y}_d(t) - k[\sum_{r=1}^{\infty} A_r(t)\Phi_r(d) - y_d(t)] + c[\sum_{r=1}^{\infty} A_r(t)\Phi_r(d) + A_r(t)\Phi_r'(d)v_d \\ - y_d(t)] = 0 \quad (26)$$

where  $S_p(t)$  and  $H_p(t)$  can be defined as:

$$S_p(t) = \int_0^L \Phi_r(x)F(x,t)dx, r = 1, 2, \dots \quad (27)$$

$$H_p(t) = \int_0^L \Phi_r(x)D(x,t)dx, r = 1, 2, \dots \quad (28)$$

and  $d$  is the position of the absorber, which corresponds to  $x_r$  for the MDR.

To determine the performance of the mobile damping robot, the energy dissipated is defined as follows:

$$E_{disp} = \int_0^{t_1} c \left[ \dot{y}_d(t) - \sum_{r=0}^{\infty} \dot{A}_r(t)\Phi(v_d t) \right]^2 dt \quad (29)$$

The efficiency of the absorber can be obtained as in [42]:

$$\eta = \frac{E_{disp}}{W} \quad (30)$$

where  $W$  is the input energy due to the external force and it can be expressed as:

$$W = \int_0^{t_1} \int_0^L F(x,t)\Phi(x)\dot{A}(t)dxdt \quad (31)$$

### 3. Numerical simulations

The numerical simulations were performed on a 200-meter span length, using 795 Drake ACSR cable. Table 1 shows the parameters of the cable as well as the applied load. The cable natural frequencies were determined and used as wind excitation inputs. Table 2 lists five natural frequencies of the cable falling within the range of Aeolian vibration. Table 3 shows the parameters of the MDR. The mass of the mobile device is taken to be 8% of the total mass of the cable. 95% of the total mass of the robot is assigned to the absorber. The MDR uses a proportional-derivative controller to move from its current position on the cable to the antinode.

#### 3.1. Validation

The model presented above was validated by comparing the numerical results of the MATLAB function 'ode45' to the analytical results of the harmonic balance method. The comparison was done for the fundamental frequency of the system. The problem was simplified by fixing the position of the device on the cable. The solution for the time function  $A(t)$  of the conductor as well as the solution of the absorber displacement can be given as follow:

$$A(t) = c_1\cos(\omega t) + c_2\sin(\omega t) \quad (32)$$

$$y_d(t) = c_3\cos(\omega t) + c_4\sin(\omega t) \quad (33)$$

Inserting these assumed solutions in the equations of motion yields

**Table 1**  
Parameters of the conductor and the applied load.

$L(m)$	$m(\text{kg/m})$	$T(N)$	$EI(\text{N.m}^2)$	$\omega_n(\text{rad/s})$	$f_0(\text{N/m})$
200	1.6286	27,840	1602	$\omega_e$	$f(V_w)$

**Table 2**

Frequencies within the range of Aeolian vibration for a 200 m cable in Hz.

$\omega_{10}$	$\omega_{20}$	$\omega_{30}$	$\omega_{40}$	$\omega_{50}$
3.21	6.56	9.87	13.22	16.63

**Table 3**

Parameters of the mobile damping robot.

$m_r(\text{kg})$	$m_d(\text{kg})$	$k(\text{N/m})$	$c(\text{Ns/m})$	$k_p$	$k_d$	$v_d(\text{m/s})$
1.3	24.8	104.4	177	1	0.5	0.1

four linear equations which can be solved using the arc-continuation method for  $c_1$ ,  $c_2$ ,  $c_3$  and  $c_4$ . Fig. 3 shows that there is excellent agreement between the analytical and numerical results with a maximum error of 1%.

#### 3.2. The effect of Coriolis on the system dynamics

In order to determine the effect of Coriolis terms in Eq. (17), the time response of the system in the presence and absence of these higher order terms are presented in Fig. 4. The findings indicate that considering these higher order terms (i.e., Coriolis acceleration) in the simulations does not have a significant impact on the response. Indeed, the curves almost coincide with each other. Fig. 4-(b) shows the percentage error between both simulations to demonstrate the effect of these terms. Yet the results further demonstrate low percentage error (i.e, less than 0.3%), thus, the higher order terms are neglected in all subsequent simulations.

#### 3.3. Determining the optimal location

The optimal location for vibration suppression corresponds to the antinodes of the conductor. For Aeolian vibration, the wind frequency input ranges from 3 Hz to 150 Hz. For this reason, the frequency analysis can be done for this range to better understand the effect of the robot position on the achieved vibration attenuation. Fig. 5 shows the frequency response of the cable (Fig. 5-(a)) and the robot (Fig. 5-(b)) at different robot positions along the cable for different wind excitation inputs. The frequency in Fig. 5 is normalized with respect to the fundamental frequency of the system. The response represents the transmissibilities (i.e., displacement amplitude over input force) in dB. When the transmissibility is 1, the corresponding value in dB is 0. For amplitudes larger than inputs the transmissibility is positive. For

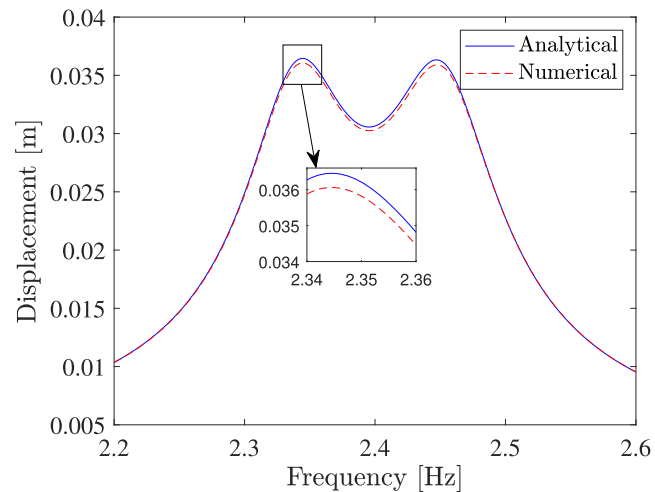
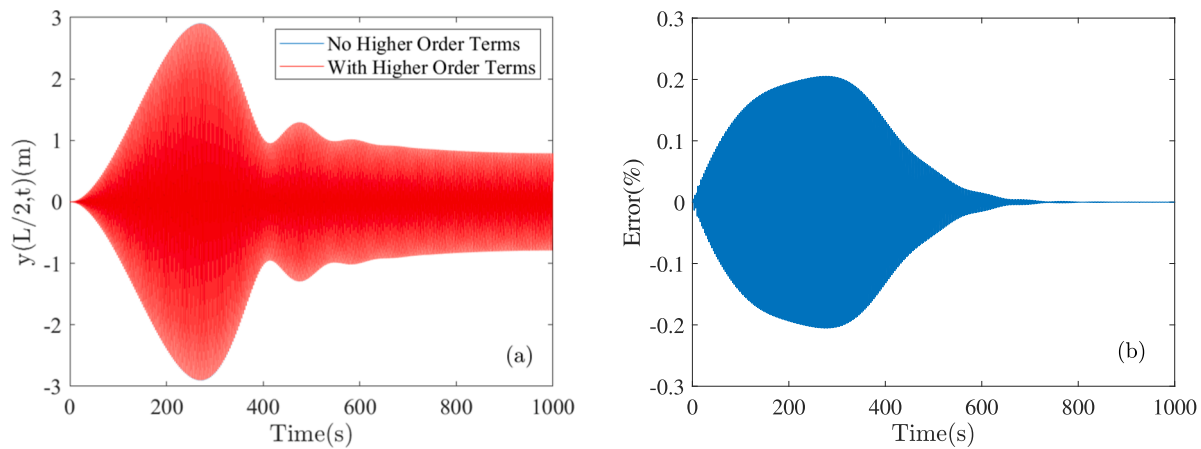
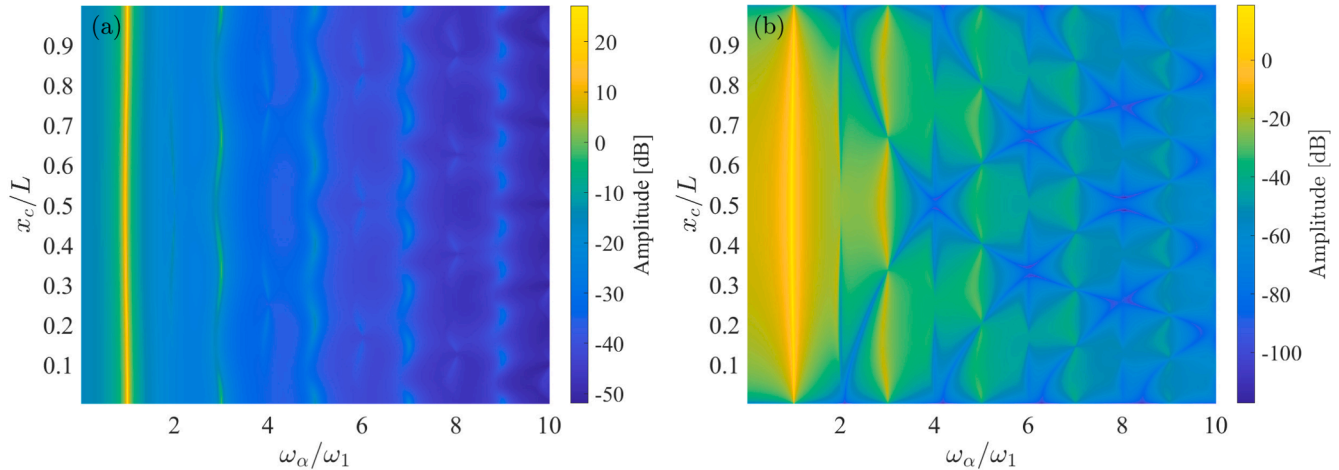


Fig. 3. A comparison between the analytical and the numerical simulation.



**Fig. 4.** Evaluating the importance of including higher order terms. Figure-(a) compares the response of the system with and without Coriolis terms. Figure-(b) shows the error between the two simulations.



**Fig. 5.** Frequency response of the cable and the robot along the span. Figure-(a) shows the transmissibility of the cable as a function of the normalized frequency. Figure-(b) shows the transmissibility of the robot as a function of the normalized frequency.

amplitudes smaller than inputs, the transmissibility is negative. The vibration of the cable depends on the robot position. If the absorber is tuned to the wind input frequency and it is properly placed at an antinode, it becomes fully effective by mitigating the vibration of the cable. On the other hand, if the absorber coincides with a node, it becomes ineffective. Consequently, a fixed TVA will be limited because there is a chance that it coincides with a node, especially at higher frequencies as shown in Fig. 5-(b). Moreover, the relevance of the mobile damping robot becomes apparent. By consistently self-adjusting its position to an antinode, the mobile damping robot can potentially increase its effectiveness.

In order to further demonstrate the significance of proper robot placement, Fig. 6 shows the response of the system at specific frequency for different robot locations. Fig. 6-(a) shows the response of the cable and the robot excited at the fundamental frequency of the bare cable. Then, Fig. 6-(b), 6-(c) and 6-(d) represent the response of the system at higher frequencies falling within the range of Aeolian vibrations. In these figures, the transmissibility of the system is plotted at each location across the span of the cable. The transmissibility represents the amplitude of the conductor over the input force expressed in dB. These figures (i.e., sub-figures of Fig. 6) are particularly useful, because they show where the robot should be placed for best performance. Moreover, they also indicate that at higher frequencies the amplitude decreases. Although higher frequencies yield low vibration amplitude, it is essential to suppress the vibration at the antinodes of these frequencies. The

reason is that frequency is proportionally related to fatigue failure. Indeed as the frequency increases, the number of cycles increases, thus potentially decreasing the lifetime of the conductor [43,44].

Fig. 7 shows the response at the midspan of the cable excited at resonance. The frequencies selected are 3 Hz, 5 Hz, 10 Hz and 20 Hz. The simulation includes up to sixty modes of expansion to capture the dynamics of the system correctly. The graph compares the performance of the fixed damper against the proposed mobile damping robot. Following Barry et al. [45] the fixed damper is installed within 85%–95% of the vibrating loop that corresponds to the highest input wind speed. For the selected cable, this indication corresponds to an optimal location between  $x = 1.14\text{--}1.27\text{m}$  which represent 0.57%–0.64% of the cable total length. This location prevents the fixed damper from coinciding with a vibration node. The proposed solution features a feedback controller for antinode tracking. The vibration suppression is maximized once the robot reaches an antinode. Because there are multiple antinodes, the robot moves from antinode to antinode until the vibration throughout the span is suppressed to a satisfactory level. The results show that for every frequency the moving damping robot outperforms the fixed absorber. The time-series response is comparable to [24] and show similar trends.

Additionally, we can also compare the performance of the fixed damper to the moving damper by evaluating the steady state displacement of the cable as presented in Fig. 8. The results show that as the wind speed increases, the overall displacement of the conductor

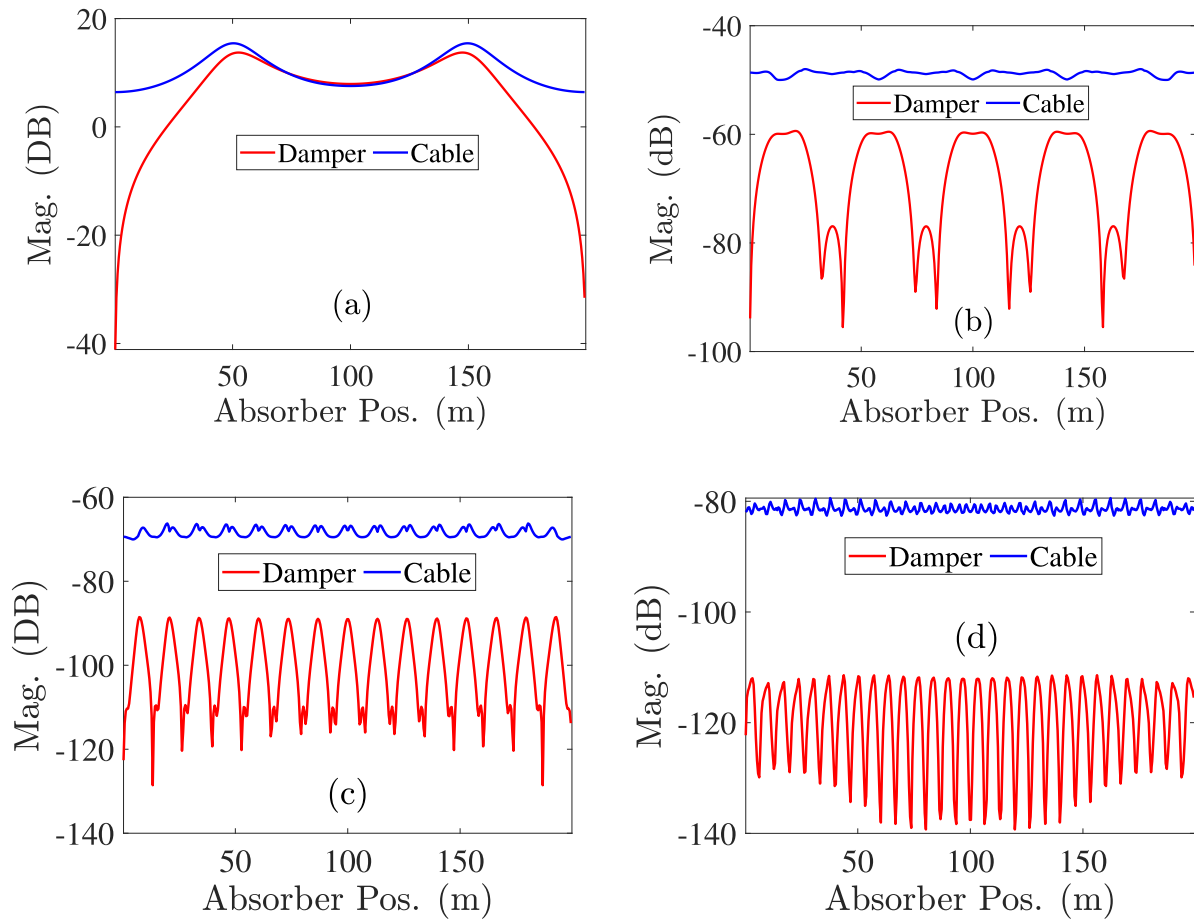


**Fig. 6.** Frequency analysis of the robot and the cable. This graph complements the previous Figure. It elucidates where to place the robot for best performance. Figure-(a),(b),(c) and (d) show the frequency response across the span of the cable for 0.3 Hz, 5 Hz, 10 Hz and 20 Hz, respectively.

increases. This trend is due to the fact that the wind speed is also proportional to the wind force. Hence as the wind speed increase, the force also increases, and consequently the vibration amplitude also increases in both cases (i.e., moving damper vs. fixed damper). However, the moving damper provides at least 30% improvement in terms of vibration reduction when compared to the fixed damper for the range of velocities between 3.5 m/s and 7 m/s.

#### 3.4. Optimizing the weight ratio between in-span mass and absorber mass

Since determining the required actuator force to drive the mobile robot is significant in controller design, the weight distribution between the robot and the absorber is another parameter of interest. The total mass of the damping robot (i.e., in-span mass holding all the electronics plus absorber mass) is assumed to be 8% [46] of the cable mass, which equate to 26.06 kg based on the previously given parameters. The total mass of the mobile damping robot is defined as  $m_t$ .  $\alpha$  is defined as the ratio of the in-span mass to the total mass of the MDR. The mass ratio of the absorber to the total mass of the MDR is, therefore, defined as  $1 - \alpha$  (i.e.,  $\beta$ ). Fig. 9 shows the effect of the mass ratio on the overall energy dissipation and the maximum amplitude of the cable. As the in-span mass increases, the maximum amplitude at the midspan increases. However, the response is almost identical at steady state for each  $\alpha$ . Fig. 9-(b) shows more specifically how the mass ratio affects the maximum displacement of the conductor. As  $\alpha$  increases, the maximum displacement of the conductor increases. However, the change in maximum amplitude is small. Furthermore, a smaller in-span mass helps the MDR reach steady state quicker, hence the in-span mass of the MDR needs to be minimized for better performance.

#### 3.5. Determining the optimal robot velocity

Velocity is a key parameter for antinode tracking. The desired velocity is provided by the signal from the PD controller. The effects of the velocity on the cable displacement and the MDR displacement are depicted in Fig. 10 and Fig. 11, respectively. This simulation is done with the wind excitation frequency matching the tenth mode of the cable (i.e 3 Hz). The vibration response is measured at the midspan. Fig. 10-(a) indicates that increasing the robot velocity has a significant effect on reducing the cable displacement. The conductor experiences lower amplitude transient response and reaches a steady vibration level faster. In terms of maximum vibration amplitude, Fig. 10-(b) shows that as the velocity of the MDR increases, the maximum vibration amplitude at the midspan decreases. However, the change is negligible. The velocity parameter can also be studied at the local position of the MDR. In this case, Fig. 11-(a) and (b) show that increasing the robot velocity increases the maximum vibration of the MDR. However, the higher the velocity the quicker the MDR reaches its target antinode. Therefore there is a tradeoff between the maximum amplitude and the time required to reach a steady state location for the MDR. This observation will be useful in determining the desired velocity of the MDR to help optimize vibration suppression throughout the span of the conductor.

#### 3.6. Determining the efficiency of the mobile damper

A strong indicator of the MDR performance is its efficiency to dissipate the energy generated by the wind force at resonance. The efficiency of the MDR can be evaluated by calculating the energy dissipated as the robot moves towards the antinode using Eq. (29). Fig. 12 summarizes

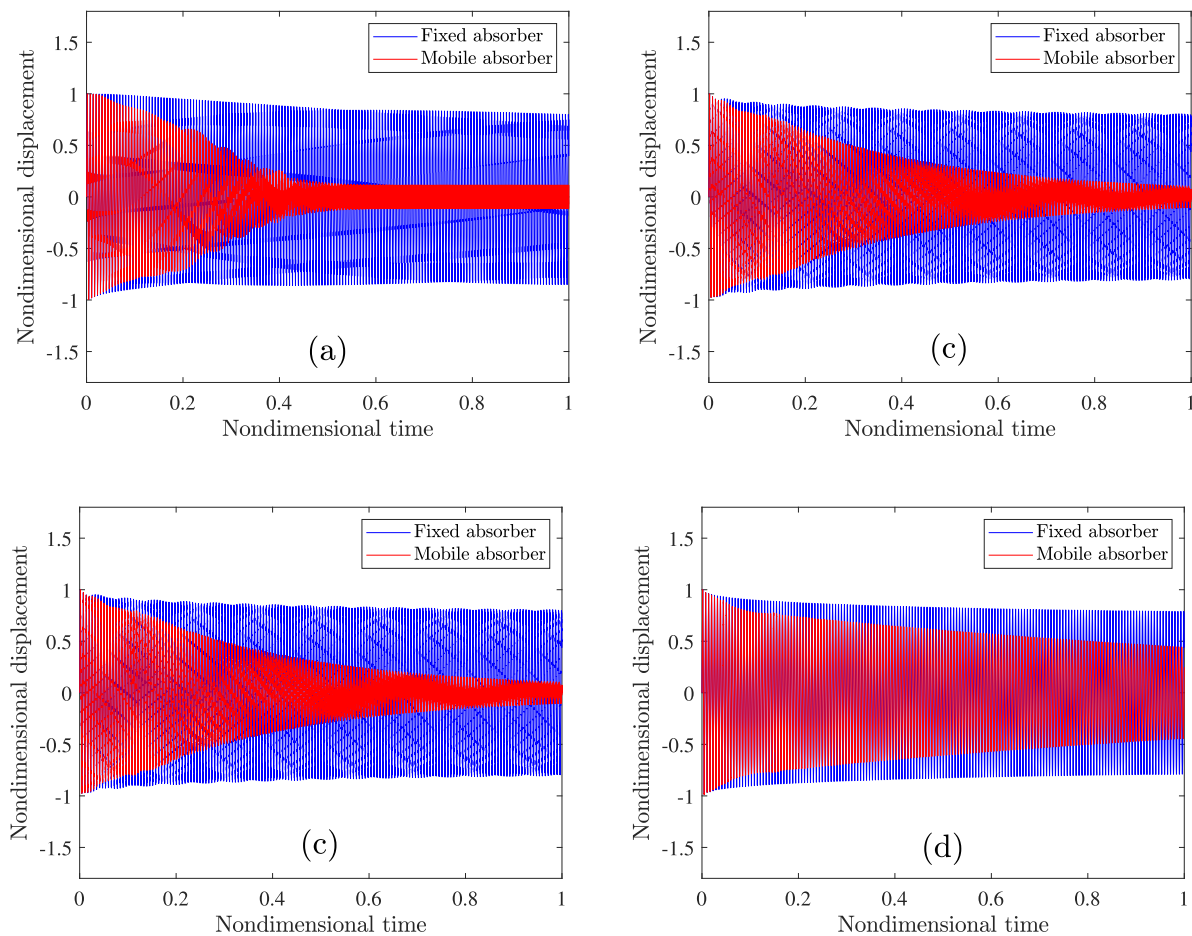


**Fig. 7.** Comparison of the fixed absorber and the MDR vibration suppression at the mid-span for different resonant frequencies. Figure-(a), (b), (c) and (d) show the response of the system for resonant frequencies 3 Hz, 5 Hz, 10 Hz and 20 Hz, respectively.

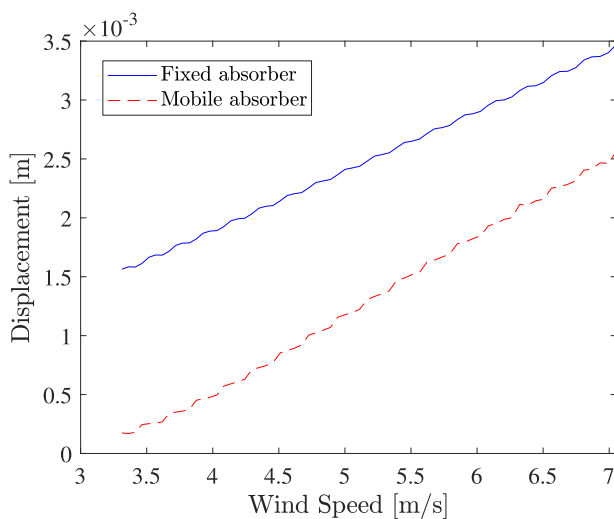


**Fig. 8.** Comparing the steady state displacement of the cable when attached to a fixed damper and a moving damper. At steady state the fixed damper is at the optimal location following the literature. The moving damper is readjusted to an antinode corresponding to the input excitation frequency.

the results for the energy and efficiency implication of the system. Fig. 12-(a) indicates that as the velocity of the robot increases, the energy dissipated through the absorber decreases. On the other hand, as the velocity increases, the efficiency of the mobile robot increases as

shown in Fig. 12-(b). These Figs. outline a key aspect of antinode tracking. That is increasing the speed enables the robot to rapidly damp the oscillation of the cable. Albeit the cable is at resonance, the displacement of the MDR towards the antinodes prevents energy build up throughout the span of the cable. This feature of the MDR decreases the amount of energy the MDR needs to dissipate. On the other hand, the effect of the suspended mass and the in-span mass is depicted in Fig. 12-(c) and Fig. 12-(d). Both Figs. demonstrate that the performance of the damping robot is enhanced with increasing suspended mass, but it is degraded with increasing in-span mass. The latter suggests that the mass of the robot constrains the robot design.

### 3.7. Required actuator force

Another important aspect of the operation of the robot is to understand the input force required to drive the robot. Fig. 13-(a) shows that the input force to the system increases with increasing velocity. Fig. 13-(b) shows the effect of the in-span mass on the required input force. The results demonstrate that increasing the in-span mass increases the required input force. These results match our intuition that higher velocity and higher robot mass require a higher power demand. Therefore, the required actuator force is an essential parameter to be considered from a design standpoint.

Finally, it is noteworthy that although the vibration suppression efficiency of the mobile damping robot increases with increasing speed, the dissipated energy in the suspended mass decreases (from Fig. 10-(b) and Fig. 12-(b)). This makes installing energy harvester to self-power the moving robot impractical for high absorber velocities. Moreover, higher velocities require higher input forces to drive the system.

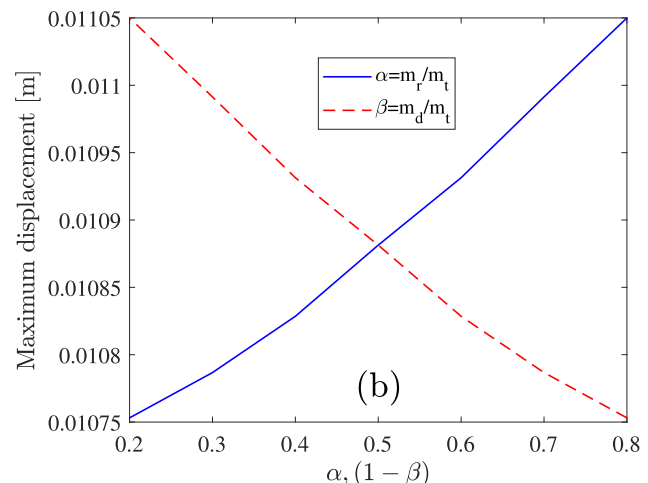
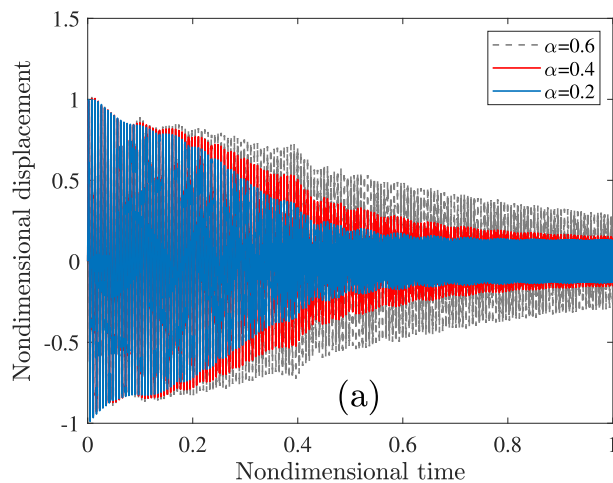


**Fig. 9.** Mass ratio study between in-span mass and absorber mass. **Fig. 8-(a)** shows the nondimensional displacement at the midspan for different mass ratio  $\alpha$  (in-span mass over total mass). **Fig. 8-(b)** shows the maximum amplitude of the cable at the midspan for  $\alpha$  and  $\beta$ .

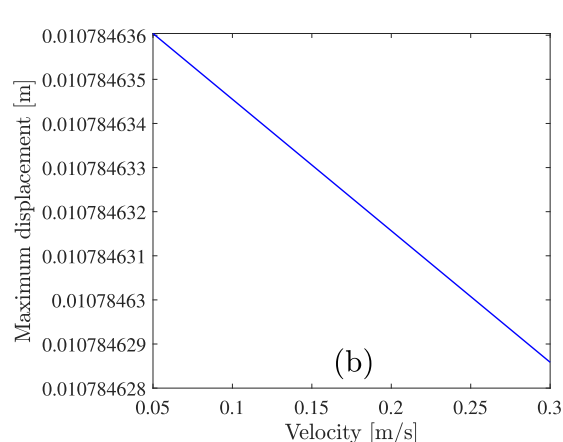
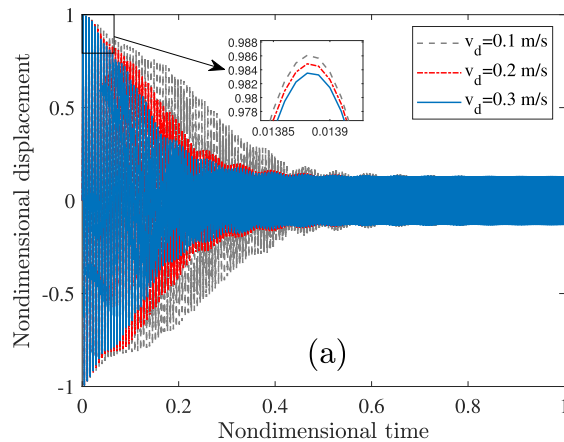


**Fig. 10.** Comparing the effect of different robot velocities at the midspan. **Fig. 9-(a)** shows the nondimensional displacement of the cable at the midspan for different MDR velocities. **Fig. 9-(b)** depicts the maximum displacement of the cable at the midspan for different velocities.

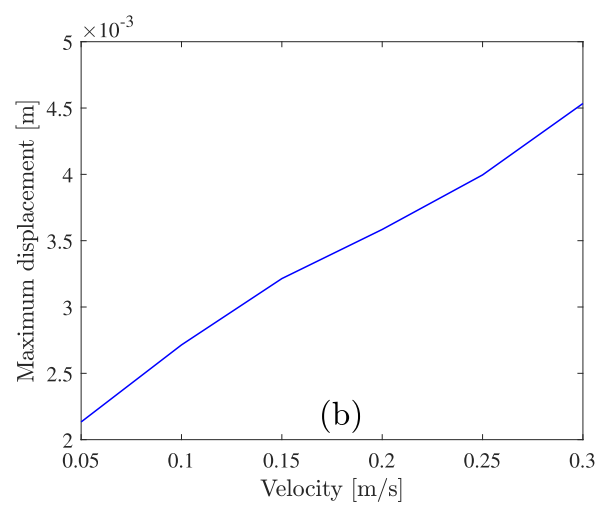
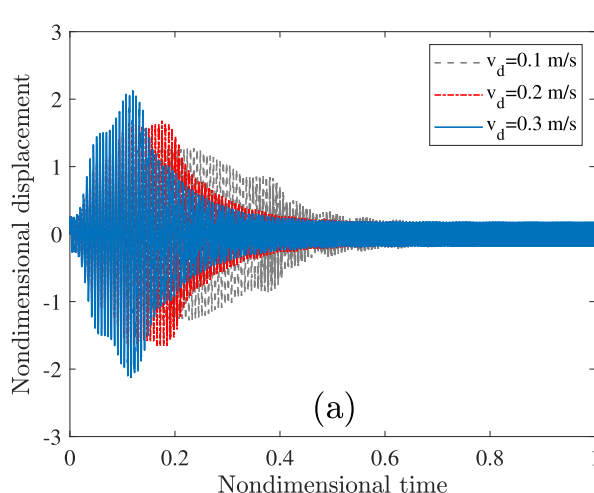


**Fig. 11.** Visualizing the effect of different robot velocities as it tracks the antinode. **Fig. 10-(a)** shows the nondimensional displacement at the local position of the MDR for different velocities. **Fig. 10-(b)** depicts the maximum displacement of the MDR for different velocities.

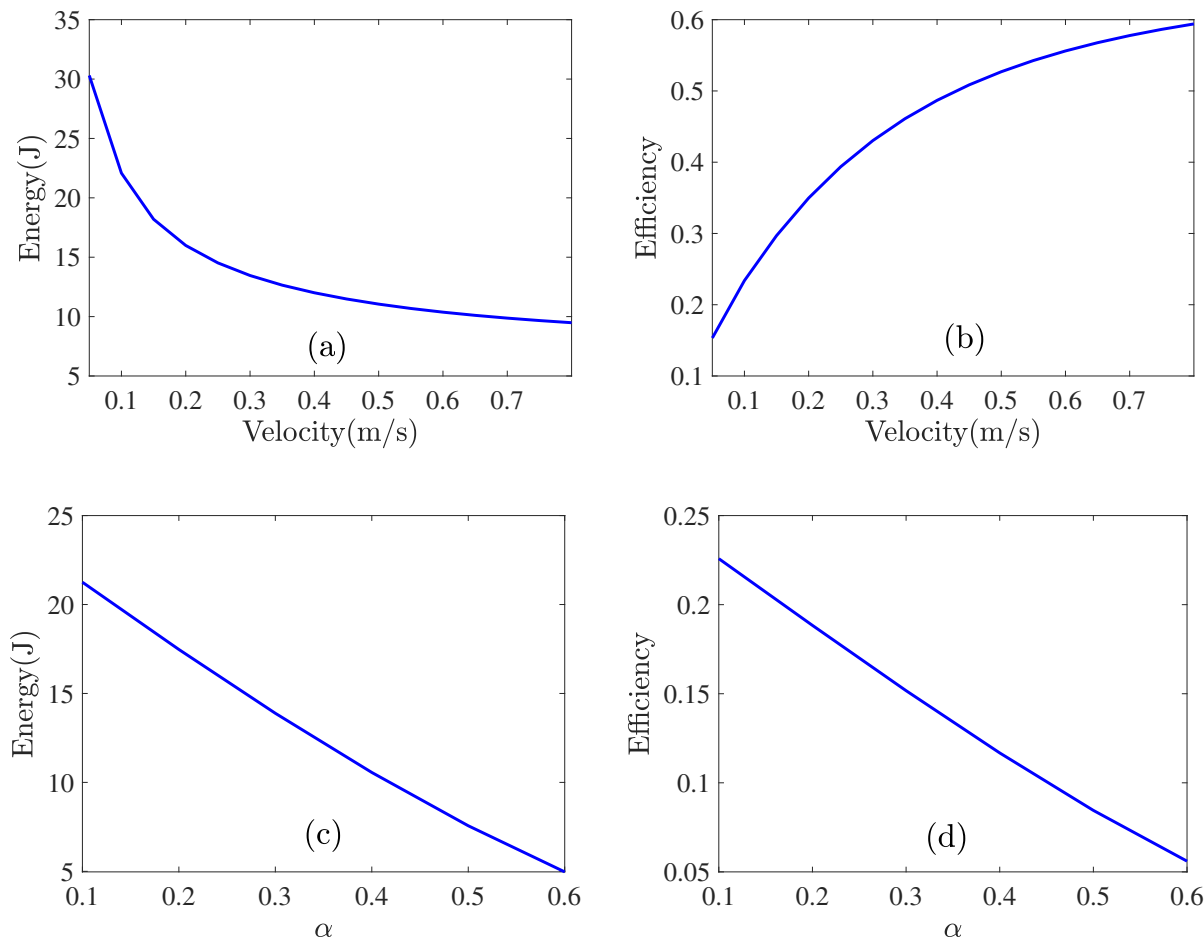


**Fig. 12.** Energy dissipation and efficiency of the mobile damping robot in terms of velocity ((a) and (b)) and mass ratio ((c) and (d)).

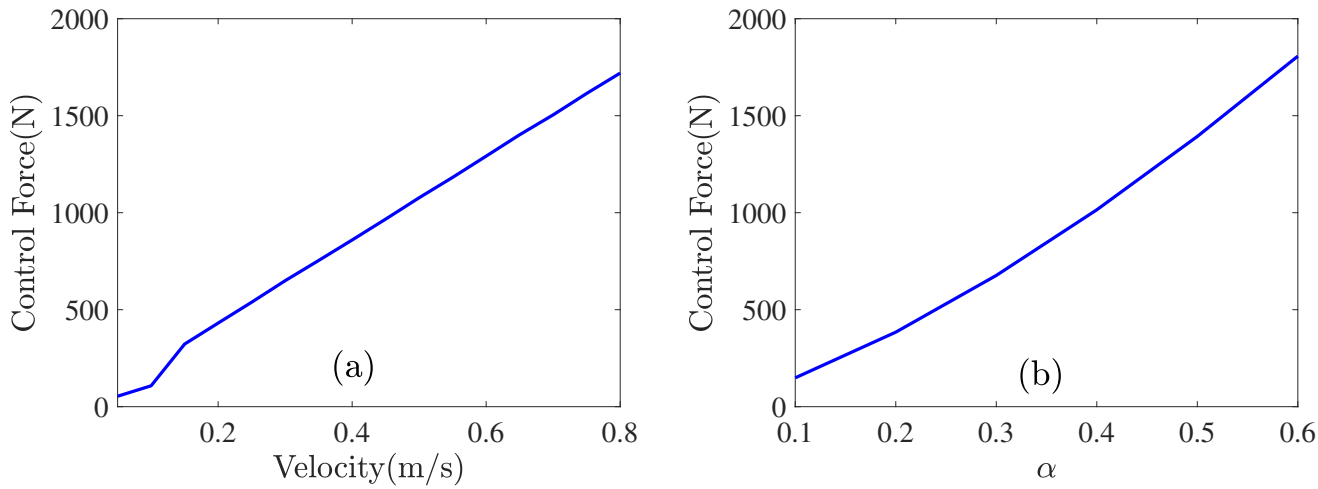


**Fig. 13.** Evaluation the control force required as a function of velocity in Fig. 12-(a) and mass ratio  $\alpha$  in Fig. 12-(b).

#### 4. Conclusions and future work

The objective of this study was to investigate the performance of an adaptive mobile damping robot for mitigating Aeolian vibration of power lines. A PD controller was used to drive the mobile device to a vibration antinode, thus maximizing the energy dissipated over a wider range of frequencies. The equations of motion of the system, accounting for the two-way nonlinear interactions of the cable and the robot, were

derived using Hamilton's Principle. The model was validated by comparing the numerical results to the analytical results obtained using the harmonic balance method. The numerical simulations demonstrated that the mobile damping robot substantially outperforms the fixed TVA at wider range of frequencies. Moreover, the simulations also revealed that the PD controller can effectively track the vibration antinode. The MDR also helped reduce the average vibration of the system for different resonant frequencies. A further parametric study was conducted to

evaluate the role of different robot parameters on the cable displacement. The parametric study showed that for optimal robot performance, the in-span mass needs to be minimized. Moreover, the velocity, the energy, and the efficiency evaluation showed that increasing the velocity enables the robot to effectively mitigate the cable vibrations. However, this increase in velocity was proportional to an increase in input control demand. It also decreased the amount of energy dissipated. This observation suggests that a decent amount of energy dissipation may present an energy harvesting opportunity. For future work, it would be of interest to develop a cost function to optimize the parameters of the robot with the help of the qualitative results obtain in the present work. Another investigation opportunity will involve trajectory mapping to the antinodes with a more detailed control framework. Finally, a complete nonlinear model including the fluid-structure interaction of the cable and mobile damping robot will be considered.

## Declaration of Competing Interest

The authors declare that they have no known competing financial interests or personal relationships that could have appeared to influence the work reported in this paper.

## Acknowledgment

This work is supported in part by the National Science Foundation (NSF) Grant ECCS-1944032: CAREER: Towards a Self-Powered Autonomous Robot for Intelligent Power Lines Vibration Control and Monitoring.

## References

- [1] Vecchiarelli J, Currie IG, Havard DG. Computational analysis of aeolian conductor vibration with a stockbridge-type damper. *J Fluids Struct* 2000;14(4):489–509.
- [2] Lu ML, Chan JK. An efficient algorithm for aeolian vibration of single conductor with multiple dampers. *IEEE Trans Power Delivery* 2007;22(3):1822–9.
- [3] Barry O, Oguamanam DCD, Lin DC. Aeolian vibration of a single conductor with a stockbridge damper. *Proc Inst Mech Engineers, Part C: J Mech Eng Sci* 2013;227(5):935–45.
- [4] Rafiou Oumar Barry. Vibration Modeling and Analysis of a Single Conductor With Stockbridge Dampers. PhD thesis, 2014.
- [5] Barry O, Zu JW, Oguamanam DCD. Analytical and experimental investigation of overhead transmission line vibration. *J Vib Control* 2015;21(14):2825–37.
- [6] Barry O, Bukhari M. On the modeling and analysis of an energy harvester moving vibration absorber for power lines. *ASME 2017 Dynamic Systems and Control Conference*. American Society of Mechanical Engineers Digital Collection 2017.
- [7] President's Council of Economic Advisers. Economic benefits of increasing electric grid resilience to weather outages. 1:163–178, 2013.
- [8] CBS International Journal of Mechanical Sciences. 4,000 dte customers remain without power nearly a week after damaging winds. 1:163–178, 2017.
- [9] Sun JQ, Re Jolly M, Norris MA. Passive, adaptive and active tuned vibration absorbers—a survey. *J Vibration Acoustics*, 117(B):234–242, 1995.
- [10] Jalili N. A comparative study and analysis of semi-active vibration-control systems. *J Vib Acoust* 2002;124(4):593–605.
- [11] Miguelez MH, Rubio L, Loya JA, Fernandez-Saez J. Improvement of chatter stability in boring operations with passive vibration absorbers. *Int J Mech Sci* 2010; 52(10):1376–84.
- [12] Tewani SG, Rouch KE, Walcott BL. A study of cutting process stability of a boring bar with active dynamic absorber. *Int J Mach Tools Manuf* 1995;35(1):91–108.
- [13] Moradi H, Bakhtiari-Nejad F, Movahhedy MR. Tuneable vibration absorber design to suppress vibrations: an application in boring manufacturing process. *J Sound Vib* 2008;318(1–2):93–108.
- [14] Malcolm John Hudson, Paul Reynolds. Implementation considerations for active vibration control in the design of floor structures. *Eng Struct* 2012;44:334–58.
- [15] Lackner MA, Roten MA. Passive structural control of offshore wind turbines. *Wind Energy* 2011;14(3):373–88.
- [16] Navid Asmari Saadabad, Hamed Moradi, Gholamreza Vossoughi. Semi-active control of forced oscillations in power transmission lines via optimum tuneable vibration absorbers: with review on linear dynamic aspects. *Int J Mech Sci*, 87: 163–178, 2014.
- [17] Liao GJ, Gong XL, Kang CJ, Xuan SH. The design of an active-adaptive tuned vibration absorber based on magnetorheological elastomer and its vibration attenuation performance. *Smart Mater Struct* 2011;20(7):075015.
- [18] Williams K, Chiu G, Bernhard R. Adaptive-passive absorbers using shape-memory alloys. *J Sound Vib* 2002;249(5):835–48.
- [19] Acar MA, Yilmaz C. Design of an adaptive-passive dynamic vibration absorber composed of a string-mass system equipped with negative stiffness tension adjusting mechanism. *J Sound Vib* 2013;332(2):231–45.
- [20] Oguamanam DCD, Hansen JS, Heppeler GR. Dynamics of a three-dimensional overhead crane system. *J Sound Vib* 2001;242(3):411–26.
- [21] Karimi AH, Ziae-Rad S. Vibration analysis of a beam with moving support subjected to a moving mass travelling with constant and variable speed. *Commun Nonlinear Sci Numer Simul* 2015;29(1–3):372–90.
- [22] Zupan E, Zupan D. Dynamic analysis of geometrically non-linear three-dimensional beams under moving mass. *J Sound Vib* 2018;413:354–67.
- [23] He W. Vertical dynamics of a single-span beam subjected to moving mass-suspended payload system with variable speeds. *J Sound Vib* 2018;418:36–54.
- [24] Samani FS, Pellicano F. Vibration reduction of beams under successive traveling loads by means of linear and nonlinear dynamic absorbers. *J Sound Vib* 2012;331(10):2272–90.
- [25] Samani FS, Pellicano F, Masoumi A. Performances of dynamic vibration absorbers for beams subjected to moving loads. *Nonlinear Dyn* 2013;73(1–2):1065–79.
- [26] Chang T-P, Lin G-L, Chang E. Vibration analysis of a beam with an internal hinge subjected to a random moving oscillator. *Int J Solids Struct* 2006;43(21): 6398–412.
- [27] Gašić' V, Zrnic' N, Obradovic' A, Bošnjak S. Consideration of moving oscillator problem in dynamic responses of bridge cranes. *FME Transactions* 2011;39(1): 17–24.
- [28] Jakšić Vesna, O'Connor Alan, Pakrashi Vikram. Damage detection and calibration from beam-moving oscillator interaction employing surface roughness. *J Sound Vib* 2014;333(17):3917–30.
- [29] Nikol O, Heics RC, Houston HJ. Aeolian vibration of single conductors and its control. *IEEE Trans Power Apparatus Syst* 1985;11:3245–54.
- [30] Stancioiu D, Ouyang H, Mottershead JE. Vibration of a beam excited by a moving oscillator considering separation and reattachment. *J Sound Vib* 2008;310(4–5): 1128–40.
- [31] Xie W, Peng T, Xiao K, Zhang J. Research advances of aeolian vibration of damper-line system. *Int J Eng Technol* 2017;9(6):437.
- [32] US EPRI and EDF R&D. Profiling and mapping of intelligent grid r&d programs. Technical report, Palo Alto, CA: US EPRI, 2006.
- [33] Oumar Barry, Zu JW, Oguamanam DCD. Nonlinear dynamics of stockbridge dampers. *J Dynamic Syst, Meas, Control*, 137(6):061017, 2015.
- [34] Vaja NK, Barry OR, Tanbour EY. On the modeling and analysis of a vibration absorber for overhead powerlines with multiple resonant frequencies. *Eng Struct* 2018;175:711–20.
- [35] Rezaei A, Sadeghi MH. Analysis of aeolian vibrations of transmission line conductors and extraction of damper optimal placement with a comprehensive methodology. *Int J Eng* 2019;31(9):328–37.
- [36] Barry O, Long R, Oguamanam DCD. Simplified vibration model and analysis of a single-conductor transmission line with dampers. *Proc Inst Mech Engineers, Part C: J Mech Eng Sci* 2017;231(22):4150–62.
- [37] Fei Jixiong, Lin Bin, Yan Shuai, Ding Mei, Xiao Juliang, Zhang Jin, et al. Chatter mitigation using moving damper. *J Sound Vib* 2017;410:49–63.
- [38] Wang YR, Lo CY. Design of hybrid dynamic balancer and vibration absorber. *Shock Vib* 2014;2014.
- [39] Bukhari Mohammad A, Barry O, Tanbour E. On the vibration analysis of power lines with moving dampers. *J Vib Control* 2018;24(18):4096–109.
- [40] Oumar Rafiou Barry, Emadeddin Y Tanbour, Nitish Kumar Vaja, and Hesham Tanbour. Asymmetric aeolian vibration damper, April 17 2018. US Patent 9,948,081.
- [41] Hagedorn P. Wind-excited vibrations of transmission lines: A comparison of different mathematical models. *Math Model* 1987;8:352–8.
- [42] Samani Farhad S, Pellicano Francesco. Vibration reduction on beams subjected to moving loads using linear and nonlinear dynamic absorbers. *J Sound Vib* 2009;325(4–5):742–54.
- [43] Li Li, Zuyan Zhang, Xu Ningbo. Research on aeolian vibration fatigue life of conductors. In: Second International Conference on Mechanics, Materials and Structural Engineering (ICMMSE 2017). Atlantis Press; 2017.
- [44] Cloutier L, ALESSANDRA MANENTI, and GIORGIO DIANA. Fatigue endurance capability of conductor/clamp systems-update of present knowledge; 2007.
- [45] Barry O, Long R, Oguamanam DCD. Rational damping arrangement design for transmission lines vibrations: analytical and experimental analysis. *J Dynamic Syst, Meas, Control*, 139(5), 2017.
- [46] Inman Daniel J, Singh Ramesh Chandra. *Engineering vibration*. NJ: Prentice Hall Englewood Cliffs; 1994.